Evidence for Higgs boson decays to a low-mass dilepton system and a photon in pp collisions at $\sqrt{s}$ = 13 TeV with the ATLAS detector

The ATLAS Collaboration

A search for the Higgs boson decaying into a photon and a pair of electrons or muons with an invariant mass $m_{\ell\ell} < 30$ GeV is presented. The analysis is performed using 139 fb^{-1} of proton–proton collision data, produced by the LHC at a centre-of-mass energy of 13 TeV and collected by the ATLAS experiment. Evidence for the $H \to \ell\ell\gamma$ process is found with a significance of 3.2σ over the background-only hypothesis, compared to an expected significance of 2.1σ. The best-fit value of the signal strength parameter, defined as the ratio of the observed signal yield to the one expected in the Standard Model, is $\mu = 1.5 \pm 0.5$. The Higgs boson production cross-section times the $H \to \ell\ell\gamma$ branching ratio for $m_{\ell\ell} < 30$ GeV is determined to be $8.7^{+2.8}_{-2.7}$ fb.

1 Introduction

In July 2012, the ATLAS and CMS Collaborations at the CERN Large Hadron Collider (LHC) announced the discovery of a new particle with a mass of approximately 125 GeV [1, 2]. Within the achieved precision, the observed properties of the particle, such as its couplings to Standard Model (SM) elementary particles, its spin and its parity, are consistent with the predictions for the SM Higgs boson [3–7].

Measurements of rare decays of the Higgs boson, such as $H \to \ell\ell\gamma$ where ℓ is an electron or muon, can probe exotic couplings introduced by possible extensions to the SM [8]. In addition, such three-body Higgs boson decays can be used to probe CP-violation in the Higgs sector [9, 10].

Multiple processes contribute to the $H \to \ell\ell\gamma$ decay (see Figure 1 for representative diagrams): Dalitz decays involving a Z boson or a virtual photon (γ^*), as well as the decay of the Higgs boson into two leptons and a photon from final-state-radiation (FSR). Their respective fractions depend on the invariant mass of the dilepton pair, $m_{\ell\ell}$. In this analysis only low-mass dilepton pairs with $m_{\ell\ell} < 30$ GeV are considered. This region is completely dominated by the decay through γ^* [8, 11, 12]. The contributions of the other processes and interferences are neglected.
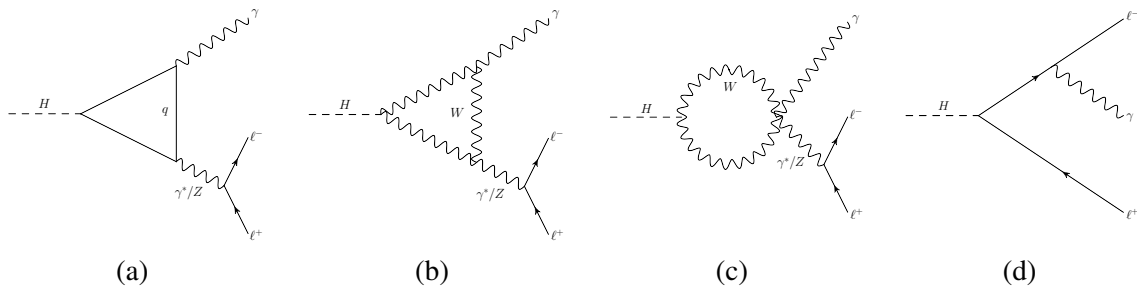

Figure 1: Representative Feynman diagrams of the $H \to \ell\ell\gamma$ process. The $H \to \ell\ell$ decay with a photon from final state radiation is shown in diagram (d).

Based on a data sample of proton–proton (pp) collisions at $\sqrt{s} = 13$ TeV with an integrated luminosity of 35.9 fb^{-1}, the CMS Collaboration reported a 95% CL upper limit on the production cross section times branching ratio for the low-mass $H \to \mu\mu\gamma$ process of 4.0 times the SM prediction [13]. In addition, both the ATLAS and CMS Collaborations carried out searches at $\sqrt{s} = 13$ TeV for the closely related $H \to Z\gamma$ process [13, 14]. The CMS Collaboration also searched for the low-mass $H \to \ell\ell\gamma$ process in the dimuon and dielectron channels in pp collisions at $\sqrt{s} = 8$ TeV [15].

This note describes a search for $H \to ee\gamma$ and $H \to \mu\mu\gamma$ decays with $m_{\ell\ell} < 30$ GeV. The search for $ee\gamma$ final states requires the development of dedicated electron trigger and identification algorithms: when the invariant mass of the two electrons is low and the transverse momentum of the dielectron system is high, their electromagnetic showers can overlap in the calorimeter.

The search uses $\sqrt{s} = 13$ TeV pp collision data recorded with the ATLAS detector during the LHC Run 2 between 2015 and 2018, corresponding to a total integrated luminosity of 139 fb^{-1}. The sensitivity of the search is enhanced by dividing the selected events into mutually exclusive categories, according to the event topology and lepton flavour. The dominant background is the irreducible non-resonant production of $\ell\ell\gamma$. After event categorisation, the signal yield is extracted by a simultaneous fit of parametric functions to the reconstructed $\ell\ell\gamma$ invariant mass ($m_{\ell\ell\gamma}$) distributions in all categories.

2 ATLAS detector

The ATLAS detector [16] covers nearly the entire solid angle around the collision point.[1] It consists of an inner tracking detector (ID) surrounded by a thin superconducting solenoid providing a 2 T axial magnetic field, electromagnetic (EM) and hadron calorimeters, and a muon spectrometer (MS). The ID covers the pseudorapidity range $|\eta| < 2.5$. It consists of silicon pixel, silicon microstrip, and transition radiation tracking detectors. The silicon pixel detector provides up to four measurements per track. The insertable B-layer (IBL) [17, 18] constitutes the innermost layer at a radius of 33.3 mm. It surrounds the beam pipe which has an inner radius of 23.5 mm. Lead/liquid-argon (LAr) sampling calorimeters provide EM energy measurements with high granularity. A steel/scintillator-tile hadron calorimeter covers the central pseudorapidity range ($|\eta| < 1.7$). The endcap and forward regions are instrumented with LAr calorimeters for both the EM and hadronic energy measurements up to $|\eta| = 4.9$. For $|\eta| < 2.5$, the EM calorimeter is divided into three longitudinal layers, which are finely segmented in η and ϕ. This segmentation allows the measurement of the lateral and longitudinal shower profile, and the calculation of shower shapes [19] used for particle identification and background rejection. The longitudinal segmentation of the EM calorimeter is also exploited to calibrate the energy response of electron and photon candidates [19]. The MS comprises separate trigger and high-precision tracking chambers measuring the deflection of muons in a magnetic field generated by superconducting air-core toroids. The precision chamber system covers the region $|\eta| < 2.7$ with three layers of monitored drift tubes, complemented by cathode-strip chambers in the forward region, where the background is highest. The muon trigger system covers the range $|\eta| < 2.4$ with resistive-plate chambers in the barrel, and thin-gap chambers in the endcap regions.

A two-level trigger system [20] was used during the $\sqrt{s} = 13$ TeV data-taking period. The first-level trigger (L1) is implemented in hardware and uses a subset of the detector information. This is followed by a software-based high-level trigger which runs algorithms similar to those in the offline reconstruction software, reducing the event rate to approximately 1 kHz from the maximum L1 rate of 100 kHz.

3 Data and simulated event samples

The analysed pp collision data at $\sqrt{s} = 13$ TeV correspond to the full recorded LHC Run-2 dataset, with an integrated luminosity of 139 fb^{-1} after the application of data quality requirements [21]. The events were collected with a combination of single-lepton, dilepton, diphoton, and lepton+photon triggers. Standard electron triggers, which require narrow, isolated EM clusters, are efficient if the two electrons in the event have a very small angular separation $|\Delta R_{ee}|$, as the two electrons produce a cluster that is similar to that of a single electron. For $|\Delta R_{ee}| > 0.1$, typically two separate EM clusters are produced. For the 2017 and 2018 data-taking periods, a dedicated trigger was introduced which requires at least one photon with $p_T > 35$ GeV and at least one EM cluster with $p_T > 25$ GeV matched to at least one ID track. The EM cluster must have low hadronic leakage but no requirement on the width of the shower is imposed, which allows this new trigger to recover a significant fraction of the signal with $0.025 < |\Delta R_{ee}| < 0.1$. More details are provided in Ref. [22]. The trigger efficiency for the $H \to ee\gamma$ and $H \to \mu\mu\gamma$ processes is 98%

---

[1] The ATLAS experiment uses a right-handed coordinate system with its origin at the nominal interaction point (IP) in the centre of the detector and the z-axis along the beam pipe. The x-axis points from the IP to the centre of the LHC ring, and the y-axis points upward. Polar coordinates (r, ϕ) are used in the transverse plane. The polar angle (θ) is measured from the positive z-axis and the azimuthal angle (ϕ) is measured from the positive x-axis in the transverse plane. The pseudorapidity is defined in as $\eta = -\ln\tan(\theta/2)$. Angular distance is measured in units of $\Delta R = \sqrt{(\Delta\eta)^2 + (\Delta\phi)^2}$.

and 96%, respectively (97% combined), relative to the event selection discussed in Section 5. As a result of the high trigger efficiency, the uncertainty in the trigger efficiency is considered negligible.

Samples of simulated Monte Carlo (MC) events are crucial for the optimisation of the search strategy and the modelling of the signal and background processes. Simulated $H \to \gamma^* \gamma \to \ell\ell\gamma$ signal and $H \to \gamma\gamma$ background events are used to parameterise these processes, and simulated non-Higgs $\ell\ell\gamma$ events are used to choose analytic functional forms to describe the non-resonant background. The generated MC events, unless stated otherwise, are processed with the full ATLAS detector simulation [23] based on GEANT4 [24]. The effect of multiple pp interactions in the same and neighbouring bunch crossings (pile-up) is included by overlaying minimum-bias events simulated with PYTHIA 8.186 [25] using the NNPDF2.3LO PDF [26] and the A3 set [27] of tuned parameters. The MC events are weighted to reproduce the distribution of the number of interactions per bunch crossing observed in the data.

Higgs boson production in the gluon–fusion (ggF) and vector-boson fusion (VBF) production modes, as well as in the quark-initiated associated production with a W or Z boson ($q\bar{q}/qg \to VH$) and with two top quarks ($t\bar{t}H$) is modelled with the POWHEG-BOX v2 MC event generator [28–32]. POWHEG-BOX v2 is interfaced with PYTHIA 8 [25] to simulate the $H \to \gamma^* \gamma \to \ell\ell\gamma$ and $H \to \gamma\gamma$ decays. PYTHIA also provides parton showering, hadronisation and the underlying event. The PDF4LHC15 parton distribution set is used [33], except for $t\bar{t}H$, where the NNPDF3.0nlo PDF set is used [26]. For the ggF process, the POWHEG NNLOPS program [34, 35] achieves next-to-next-to-leading order (NNLO) accuracy in QCD for inclusive observables after reweighting the Higgs boson rapidity spectrum [36]. The simulation reaches next-to-leading order (NLO) accuracy in QCD for the VBF, VH, and $t\bar{t}H$ processes. For VH, the MiNLO technique [37–39] is applied. No simulated samples are available for the gluon-initiated associated production with a Z boson ($gg \to ZH$) and the associated production with two b-quarks (bbH). Their minor contribution, 1% of the expected Higgs boson production, is taken into account by scaling the $q\bar{q}/qg \to ZH$ and ggF samples respectively, according to the respective cross sections.

Alternative $H \to \gamma\gamma$ samples are considered for the ggF and VBF processes. HERWIG 7 [40] instead of PYTHIA 8 is used to provide parton showering. Weights are calculated by comparing the truth-level Higgs boson transverse momentum and jet distributions in these samples to the distributions obtained from the nominal $H \to \gamma\gamma$ samples. The weights are applied to the $H \to \gamma^* \gamma \to \ell\ell\gamma$ ggF and VBF samples to estimate the effect of variations in the parton shower and underlying event.

The mass of the Higgs boson is set in the simulation to $m_H = 125$ GeV and its width to $\Gamma_H = 4.1$ MeV [41]. The Higgs mass peak position in the simulation is corrected to account for the fact that the samples are not simulated at 125.09 GeV [42] (see Section 6), otherwise the effect on the kinematics is neglected.

The signal and $H \to \gamma\gamma$ samples are normalised with the best available theoretical calculations of the corresponding SM production cross sections at $m_H = 125.09$ GeV, which are available at next-to-next-to-next-to leading order (N3LO) in QCD with NLO electroweak (EW) corrections for ggF [41, 43–54], approximate-NNLO in QCD with NLO EW corrections for VBF [41, 55–57], NNLO in QCD with NLO EW corrections for $q\bar{q}/qg \to VH$ [41, 58–65] and NLO in QCD with NLO electroweak corrections for $t\bar{t}H$ [41, 66–69]. The accuracy of the calculation is NNLO in QCD for bbH [70–72], and NLO in QCD with next-to-leading-logarithm (NLL) corrections for $gg \to ZH$ [41, 61].

There are multiple calculations of the $H \to \ell\ell\gamma$ branching ratios for different slices of phase space [8, 11, 12, 73–76]. The $H \to \ell\ell\gamma$ branching ratios used in this analysis are $\mathcal{B}(H \to ee\gamma) = 7.20 \times 10^{-5}$ and $\mathcal{B}(H \to \mu\mu\gamma) = 3.42 \times 10^{-5}$, as estimated with PYTHIA 8 for $m_{\ell\ell} < 30$ GeV. Their sum corresponds to ~5% of the $H \to \gamma\gamma$ branching ratio. When extrapolated to a common phase space, the PYTHIA8 estimate agrees with the predictions of Refs. [74, 76] within 3%. Currently, no theoretical uncertainty calculation

exits for the low-$m_{\ell\ell}$ $H \to \ell\ell\gamma$ branching ratio. Therefore, the theoretical uncertainties in the $H \to \gamma\gamma$ and $H \to Z\gamma$ branching ratios are considered as lower and upper bounds, respectively [12], and a conservative 5.8% uncertainty is used, which corresponds to the uncertainty in the $H \to Z\gamma$ branching ratio [41].

The background originates predominantly from non-resonant $\ell\ell\gamma$ production. Events were simulated with the SHERPA 2.2.8 [77] generator based on LO matrix elements for $\ell\ell\gamma$ production with up to three additional partons and using the NNPDF3.0 PDF set [78]. The SHERPA simulation includes parton shower, fragmentation and underlying-event modelling. As the statistical uncertainties in the simulated $\ell\ell\gamma$ background samples are a limiting factor when studying the background modelling at the level required by the small expected signal, a procedure was developed to generate significantly larger samples. These are based on events generated using the SHERPA 2.2.8 configuration described above with object efficiencies approximated by parameterisations rather than using the full ATLAS detector simulation and reconstruction software. The parameterisations, extracted from fully simulated MC samples, reproduce the reconstruction and selection efficiencies of detector-level objects via event weighting. Comparisons with a sample that underwent the full ATLAS detector simulation show good agreement within the statistical uncertainties.

4 Object selection

Events are required to have a collision vertex associated with at least two tracks with transverse momentum $p_{\mathrm{T}} > 0.5$ GeV each. In the case of multiple vertices, the vertex with the largest $\sum p_{\mathrm{T}}^2$ of the associated tracks is considered as the primary vertex.

Muon candidates are obtained by matching high-quality tracks in the MS and ID. Stand-alone MS tracks are used to extend the muon reconstruction beyond the ID acceptance to the region of $2.5 < |\eta| < 2.7$. Muon candidates are required to satisfy the *medium* identification criteria [79, 80], be within $|\eta| < 2.7$ and have $p_{\mathrm{T}} > 3$ GeV. Muon candidates with an associated ID track must be matched to the primary vertex by having a longitudinal impact parameter Δz_0 that satisfies $|\Delta z_0 \cdot \sin\theta| < 0.5$ mm, where θ is the polar angle of the track. The significance of the transverse impact parameter d_0 calculated relative to the measured beam-line position is required to be $|d_0|/\sigma_{d_0} < 3$, where σ_{d_0} is the uncertainty in d_0. A subset of the muon candidates is also required to be isolated from additional activity in the tracking detector and in the calorimeters, using a loose isolation selection [79, 80]. The efficiency of the muon reconstruction and identification, as well as the momentum calibration, including the associated systematic uncertainties, is estimated as described in Refs. [79, 80].

Photon and electron candidates are reconstructed from energy clusters in the calorimeters which are formed using a dynamical, topological cell clustering-based algorithm [19]. Candidates in the transition region between the barrel and endcap EM calorimeters, $1.37 < |\eta| < 1.52$, are excluded. The performance of the electron and photon reconstruction, including the associated systematic uncertainties, is studied in Ref. [19].

Photon candidates can be either unconverted or converted. In the latter case, a track or conversion vertex is matched to the EM cluster. Photon candidates are required to satisfy $p_{\mathrm{T}} > 20$ GeV, $|\eta| < 2.37$, and pass the *tight* identification criteria [19, 81] as well as a loose isolation selection [19].

The energy of the EM clusters associated with the photon and electron candidates is corrected in successive steps using a combination of simulation-based and data-driven correction factors [19]. The simulation-based calibration regression is optimised separately for electrons, unconverted and converted photons. The resolution of the energy response is corrected in the simulation to match the resolution observed in data

using $Z \to ee$ events, by adjusting the electron energy such that the width of the simulated Z-boson peak matches the width observed in data.

Because of the event kinematics of the signal process, it is common that the energy deposits of the two electrons in the EM calorimeter are reconstructed as a single cluster. Therefore, two types of candidates are defined, each with its own selection criteria: one in which a topological cluster is associated with one selected ID track (*resolved* electron [82]), representing a single electron, and one in which a topological cluster is associated with two selected ID tracks (*merged ee*), representing a merged electron pair. Each considered ID track must satisfy $|\Delta z_0 \cdot \sin\theta| < 0.5$ mm and $|d_0|/\sigma_{d_0} < 5$. Resolved electron candidates are required to satisfy the *medium* likelihood-based identification criteria [19, 82], have $p_T > 4.5$ GeV and be within $|\eta| < 2.47$. A subset of the resolved electron candidates is also required to pass a loose isolation requirement [19].

ID tracks considered for merged electrons must have opposite charge, $p_T > 5$ GeV, $|\eta| < 2.5$, and at least 7 hits in the pixel and microstrip detectors combined. To suppress backgrounds from converted photons, tracks must also have a hit in the innermost pixel layer, and merged-electron candidates are rejected if they match a conversion vertex with a radius larger than 20 mm whose momentum agrees with the cluster energy. Because the kinematic behaviour of merged electrons in the calorimeter most closely resembles a photon converting early, the energy of the merged-*ee* object is calibrated as a converted photon with a conversion radius set to $r_{\text{conv}} = 30$ mm calculated relative to the measured beam-line position. As presented in Figure 2 (a), this treatment is found to introduce minimal bias to the di-electron energy measurement. To cover remaining differences between the simulated detector response to converted photons and merged-*ee* objects, the quadratic difference between the energy resolution of converted photons and merged-*ee* objects in the MC simulation is treated as an additional energy resolution uncertainty. The four-momentum of the merged-*ee* candidate is constructed using the calibrated energy and the direction and invariant mass from the vertex reconstructed from the two electron-track candidates [83].

Merged-*ee* candidates are required to have $|\eta| < 2.37$ (excluding $1.37 < |\eta| < 1.52$), $p_T > 20$ GeV and satisfy dedicated identification requirements, as the standard electron criteria have a low efficiency for objects with close-by energy deposits or broader EM showers. For the merged-*ee* identification, a multivariate discriminator is trained to separate the $\gamma^* \to ee$ signal objects from jets or single electrons. The input variables for the training include shower shape variables [82], the information provided by the transition radiation tracker [84], and the kinematic information from the cluster and ID tracks. Merged-*ee* candidates are also required to pass a tight isolation requirement [19]. A combined efficiency of ~50% for the merged-*ee* identification and isolation is achieved for $H \to \gamma^* \gamma \to ee\gamma$ events. Since photons with a relatively small conversion radius offer a similar signature as merged-*ee* objects, the merged-*ee* identification and isolation efficiency is measured in data using a tag-and-probe method with FSR photons from Z-boson radiative decays ($Z \to \ell\ell\gamma$). Candidate $Z \to \ell\ell\gamma$ events are selected with a similar selection as in Ref. [81]. Only two-track converted photons with $r_{\text{conv}} < 160$ mm, corresponding to the conversion inside the silicon pixel detector volume, are considered. The $Z \to \ell\ell\gamma$ and background yields are estimated from a fit to the $m_{\ell\ell\gamma}$ distribution in data. The extracted efficiencies are compared to the efficiencies estimated from simulated $Z \to \ell\ell\gamma$ events as shown in Figure 2 (b) for photons with $|\eta| < 0.8$. The resulting p_T- and η-dependent data/MC scale factors are between 0.9 and 1.1 and are used to correct the identification and isolation efficiencies of the simulated $H \to \gamma^* \gamma \to ee\gamma$ events. The statistical uncertainties on the scale factors are taken into account. In addition, a systematic uncertainty is assessed for the background modelling by varying the selection criteria of the $m_{\ell\ell\gamma}$ background template. The total uncertainty reaches 2% for $20 < p_T < 30$ GeV and 9% for $p_T > 50$ GeV. Figure 2 (b) also shows the comparison of the extracted efficiencies with efficiencies in simulated $H \to \gamma^* \gamma \to ee\gamma$ events where an

additional generator-level requirement of $|\Delta\eta_{ee}| < 0.003$ is used. This requirement is applied in order to better match the signal signature to the converted photon signature in the detector and approximately 70% of the merged-*ee* objects in the signal sample pass it. The efficiencies of converted photons and the merged-*ee* objects agree within 10% for $p_T < 30$ GeV and within 5% for $p_T > 30$ GeV in the entire η range.
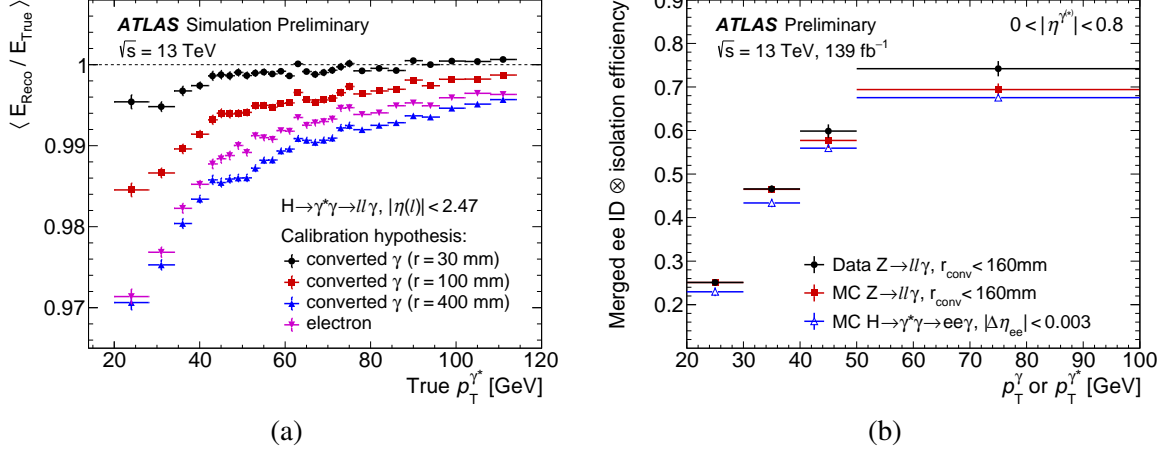

(a) (b)

Figure 2: (a) Ratio of reconstructed to true merged-*ee* energy in simulated $H \rightarrow \gamma^*\gamma \rightarrow ee\gamma$ events as a function of the true merged-*ee* p_T for several energy calibration techniques. The merged-*ee* object is calibrated as a photon with a conversion radius of 30 mm (black, analysis choice), 100 mm (red), and 400 mm (blue) or as an electron (purple). (b) Combined merged-*ee* identification and isolation efficiency extracted from $Z \rightarrow \ell\ell\gamma$ events with a photon that coverts within a radius of $r_{conv} < 160$ mm. The efficiencies are shown for photons with $|\eta| < 0.8$ as a function of p_T. Data (black) are compared with simulated $Z \rightarrow \ell\ell\gamma$ events (red). The resulting efficiencies are also compared with efficiencies in simulated $H \rightarrow \gamma^*\gamma \rightarrow ee\gamma$ events (blue). On all points, the vertical error bars indicate the statistical uncertainties.

Jets are reconstructed from topological clusters [85] using the anti-k_t algorithm [86] with a radius parameter of 0.4 and are required to have $p_T > 20$ GeV and $|\eta| < 4.4$. Jets produced in pile-up interactions are suppressed by requiring that those with $p_T < 60$ GeV and $|\eta| < 2.4$ pass a selection based on a jet vertex tagging algorithm [87].

5 Event selection

Candidate $H \rightarrow \gamma^*\gamma \rightarrow \ell\ell\gamma$ events must have at least one reconstructed photon, and at least one opposite-charge, same-flavour pair of leptons (muons or resolved electrons) or one merged-*ee* object. One of the muons (resolved electrons) in the lepton pair must have $p_T > 11$ (13) GeV, to match the p_T thresholds used in the dilepton triggers. As discussed above, the merged-*ee* p_T is required to be larger than 20 GeV. If the leading photon overlaps with one of the EM clusters (resolved electrons or merged-*ee*) forming the γ^* candidate within $\Delta R < 0.02$, the photon is discarded and the next-highest-p_T photon is considered. No isolation requirement is applied to the subleading lepton (muon or resolved electron) as it is within the isolation cone of the leading lepton in the majority of events. Additionally, if the subleading lepton (muon or electron) falls within the isolation cone of the leading lepton, it is not included in the calculation of the isolation variable.

Muon pairs are given the highest priority if there are lepton pairs of different flavours in one event. If no opposite-charge muon pair satisfying the requirements above is found, the electron pair candidates are considered. The resolved electron pair, or merged-ee object with the highest vector-sum p_T of the associated ID tracks is selected.

In order to suppress events arising from FSR processes, events are rejected if the photon is within a $\Delta R = 0.4$ cone of the selected leptons. If the axis of a jet is within $\Delta R = 0.4$ around the photon or a muon, or within $\Delta R = 0.2$ of an electron (merged or resolved), the jet is discarded. However, if the electron-jet angular distance is $0.2 < \Delta R < 0.4$, the electron and therefore the event is discarded.

To suppress events involving Z-boson decays, the dilepton mass pair must satisfy $m_{\ell\ell} < 30$ GeV. To remove $J/\psi \to \ell\ell$ production, events with an invariant mass of the muon (electron) pair between 2.9 GeV $< m_{\mu\mu} <$ 3.3 GeV (2.5 GeV $< m_{ee} <$ 3.5 GeV) are excluded. Similarly, events with a dilepton mass in the range 9.1 GeV $< m_{\mu\mu} <$ 10.6 GeV (8.0 GeV $< m_{ee} <$ 11.0 GeV) are rejected to avoid $\Upsilon(nS) \to \ell\ell$ contamination.

The invariant mass of the $\ell\ell\gamma$ system is required to satisfy 110 GeV $< m_{\ell\ell\gamma} <$ 160 GeV. Additionally, the photon and dilepton momenta both must satisfy $p_T > 0.3 \cdot m_{\ell\ell\gamma}$.

The selected events are classified into mutually exclusive categories, depending on the lepton types and event topologies. The VBF-enriched categories, which have the best expected signal-over-background ratio, but the lowest event count, are defined as follows: events must contain at least two jets with $p_T > 25$ GeV. If the leading or subleading jet is a forward jet (defined as a jet with $|\eta| > 2.5$), it is required to have $p_T > 30$ GeV to suppress cases in which jets originate from pile-up. In addition, the invariant mass of the two leading jets, m_{jj}, must be greater than 500 GeV, and the pseudorapidity separation between the two leading jets, $|\Delta\eta_{jj}|$, greater than 2.7. The quantity $|\eta_{\ell\ell\gamma} - 0.5(\eta_{j1} + \eta_{j2})|$ [88] is required to be less than 2.0, where $\eta_{\ell\ell\gamma}$ is the pseudorapidity of the $\ell\ell\gamma$ system and η_{j1} (η_{j2}) is the pseudorapidity of the leading (subleading) jet. The selected leptons and the photon must be separated from the two jets by $\Delta R > 1.5$. Additionally, the azimuthal separation between the $\ell\ell\gamma$ system and the system formed by the two jets must be greater than 2.8.

The p_{Tt} is defined as the component of the transverse momentum of the $\ell\ell\gamma$ system that is perpendicular to the difference of the 3-momenta of the dilepton system and the photon candidate ($p_{Tt} = |\vec{p}_T^{\,\ell\ell\gamma} \times \hat{t}|$, where $\hat{t} = (\vec{p}_T^{\,\ell\ell} - \vec{p}_T^{\,\gamma})/|\vec{p}_T^{\,\ell\ell} - \vec{p}_T^{\,\gamma}|$). This quantity is strongly correlated with the transverse momentum of the $\ell\ell\gamma$ system, but has better experimental resolution [89, 90]. Events failing the VBF-enriched selection, but having $p_{Tt} > 100$ GeV, are classified as the high-p_{Tt} category, which has a worse expected signal-over-background ratio than the VBF-enriched category, but more expected events. The high-p_{Tt} category is expected to have an increased fraction of VBF and VH events as these production modes lead on average to higher Higgs boson p_T than ggF production.

By far, most selected events do not fall into the VBF-enriched or high-p_{Tt} categories discussed above, and are placed into the low-p_{Tt} category. The full list of all categories considered in the analysis, together with the expected yields for a 125.09 GeV Higgs boson decaying into $\ell\ell\gamma$, is shown in Table 1. The table also summarises the observed number of events in data in the $m_{\ell\ell\gamma}$ mass range of 110–160 GeV.

Table 1: Number of data events selected in each analysis category in the $m_{\ell\ell\gamma}$ mass range of 110–160 GeV. In addition, the following numbers are given: number of $H \rightarrow \gamma^*\gamma \rightarrow \ell\ell\gamma$ events in the smallest $m_{\ell\ell\gamma}$ window containing 90% of the expected signal (S_{90}), the non-resonant background in the same interval (B_{90}^N) as estimated from fits to the data sidebands using the background models described in Section 6, the resonant background in the same interval ($B_{H\rightarrow\gamma\gamma}$), the expected signal purity $f_{90} = S_{90}/(S_{90} + B_{90})$, and the expected significance estimate defined as $Z_{90} = \sqrt{2((S_{90} + B_{90}) \ln(1 + S_{90}/B_{90}) - S_{90})}$ where $B_{90} = B_{90}^N + B_{H\rightarrow\gamma\gamma}$.

Category	Events	S_{90}	B_{90}^N	$B_{H\rightarrow\gamma\gamma}$	f_{90} [%]	Z_{90}
ee resolved VBF-enriched	10	0.4	1.6	0.009	20	0.3
ee merged VBF-enriched	15	0.8	2.0	0.07	27	0.5
$\mu\mu$ VBF-enriched	33	1.3	5.9		18	0.5
ee resolved high-$p_{\mathrm{T}t}$	86	1.1	12	0.02	9	0.3
ee merged high-$p_{\mathrm{T}t}$	162	2.5	18	0.2	12	0.6
$\mu\mu$ high-$p_{\mathrm{T}t}$	210	4.0	34		11	0.7
ee resolved low-$p_{\mathrm{T}t}$	3713	22	729	0.5	2.9	0.8
ee merged low-$p_{\mathrm{T}t}$	5103	29	942	2	3.0	1.0
$\mu\mu$ low-$p_{\mathrm{T}t}$	9813	61	1750		3.4	1.4

6 Signal and background modelling

To extract the observed signal yield, parametric functions are chosen to model the $\ell\ell\gamma$ invariant mass distributions of signal and background in each analysis category. A combined model is built from these functions and fit to the selected data in the $m_{\ell\ell\gamma}$ range of 110−160 GeV, simultaneously in all categories.

The signal model, including its parameters, is obtained by fitting a Double-Sided Crystal Ball function (DSCB) [91, 92] to the $m_{\ell\ell\gamma}$ distribution obtained from the $H \rightarrow \gamma^*\gamma \rightarrow \ell\ell\gamma$ samples described in Section 3 after applying the categorisation and event selection from Section 5. The DSCB function features a Gaussian core and asymmetric power law tails. A shift of +0.09 GeV is applied to the mean of the Gaussian to account for the fact that the sample assumes a Higgs-boson mass of 125 GeV. The effective signal mass resolution, defined as half the width containing 68% (90%) of the signal events depends on the category and lies between 1.6 (2.8) GeV (*ee*-merged high-$p_{\mathrm{T}t}$ category) and 2.2 (4.0) GeV (*ee*-resolved low-$p_{\mathrm{T}t}$ category).

The $H \rightarrow \gamma\gamma$ process, which contributes as background to the electron categories through converted photons, is modelled using the same functions and parameters as the signal in the respective categories, and is scaled by the expected $H \rightarrow \gamma\gamma$ yield. The parameterisations are compatible with the statistically limited distributions obtained from simulated $H \rightarrow \gamma\gamma$ events. This background contribution is relatively small (<2.5% and <7% of the expected $H \rightarrow \gamma^*\gamma \rightarrow \ell\ell\gamma$ signal in the *ee*-resolved and *ee*-merged channel, respectively) and is taken into account in the fitting procedure.

The non-resonant background is also estimated with parametric functions. The background normalisation and function parameters are allowed to float when fitted the data. The functional forms are chosen based on background templates that are built taking into account the contribution of different processes to the background. The function choice is performed separately for each category.

The dominant part of the background originates from the non-resonant $\ell\ell\gamma$ process. There is also a smaller background from events with mis-identified photons, electrons, or muons. To estimate the fraction of events with a mis-identified photon, a control region is formed based on the signal selection,

but dropping the photon isolation requirement and using it as a discriminating variable in a template fit. A background template enriched in events with mis-identified photons is built by inverting the photon identification selection, with the prompt photon contamination removed using simulated events. The template normalisation is obtained in the background-dominated sideband of the photon isolation distribution for each category separately. In the signal region, about 10% of all selected events have a mis-identified photon, independently of the category. The fraction of events with a mis-identified electron or muon that is in fact a hadronic jet, a lepton from heavy-flavour decays or an electron from a photon conversion, is estimated in a similar manner, using a control region in which the isolation selection is dropped for the softer lepton. The estimated fractions of events with mis-identified leptons are 4% in the $\mu\mu$ low-p_{Tt} category, 2% in the ee-merged low-p_{Tt} category, and 30% in the ee-resolved low-p_{Tt} category. The latter events are separated into two cases depending on the angular distance between the electrons, as two populations with different fake rates and mass distributions were found. The numbers in the other categories are extracted as well, but suffer from fairly large statistical uncertainties.

The invariant mass template of the non-resonant $\ell\ell\gamma$ background is built from the simulated events described in Section 3. The invariant mass templates for events with mis-identified objects are obtained from background-dominated control regions, and scaled by the yields derived above. Reasonable agreement is achieved comparing the templates containing the sum of all backgrounds to the sidebands of the $m_{\ell\ell\gamma}$ distributions in data (105−120 GeV and 130−160 GeV).

The choice of fit function for the non-resonant background is made in each category using signal-plus-background fits to the constructed background-only template by measuring the bias associated to each function (the number of fitted signal events) and choosing the function with the smallest number of degrees of freedom that satisfies the bias criteria described below.

The functional forms used to model the background are selected from the following: exponential ($e^{\alpha m_{\ell\ell\gamma}}$), exponential of a second-order polynomial ($e^{\alpha m_{\ell\ell\gamma} + \beta m_{\ell\ell\gamma}^2}$), and a power-law function ($m_{\ell\ell\gamma}^\alpha$), where α and β are free parameters. Signal hypotheses with m_H ranging from 121 GeV to 129 GeV are tested in steps of 1 GeV, and the fit bias is evaluated as the absolute maximum bias over this range (referred to as the "spurious signal" in the following), similar to what is done in Ref. [1]. A function passes the test if the spurious signal is less than 10% of the expected number of $H \to \gamma^*\gamma \to \ell\ell\gamma$ events or less than 20% of the statistical uncertainty on the fitted spurious signal. To account for statistical fluctuations in the background template, the criteria are relaxed by the statistical uncertainty due to the template. Furthermore, in a background-only fit of the template in the mass range 110 GeV $< m_{\ell\ell\gamma} <$ 160 GeV, the function must pass a χ^2 test with a probability larger than 1%. As described in Ref. [93], an additional check is performed by fitting the chosen function as well as a function of the same family with one more degree of freedom to the sidebands of the $m_{\ell\ell\gamma}$ distribution in data, to ensure the data does not prefer the more complex function. Following the procedure describe above, the power-law function is selected for all categories, except for the $\mu\mu$ low-p_{Tt} and ee-merged low-p_{Tt} categories, which are best described by the second-order exponential polynomial, and the ee-resolved VBF-enriched category, for which the exponential function is chosen.

An unbinned extended likelihood function is formed from the product of the parameterised signal-plus-background probability density function of each category. Systematic uncertainties are considered in the form of nuisance parameters with Gaussian or log-normal constraints. They are correlated across all categories, except for the spurious signal uncertainties. The latter are implemented for each category as a signal-like component with a yield parameter that is constrained by a Gaussian centred at zero and a width corresponding to the estimated spurious signal. The Higgs boson mass is set to 125.09 ± 0.24 GeV [42]. The parameter of interest is the signal strength μ, which is defined as the ratio of the measured signal yield

over the SM expectation. The corresponding profile likelihood ratio is maximised to extract the best-fit μ [94]. A possible excess over the background-only hypothesis is quantified by a p-value using the profile likelihood ratio, evaluated for a vanishing $H \to \ell\ell\gamma$ branching ratio, as a test statistic. The procedure uses the asymptotic approximation [94]. With some adjustments to the included theory uncertainties (see Section 7) and assuming SM acceptances, the measurement of the signal strength can be converted into a measurement of the Higgs boson production cross-section times the $H \to \ell\ell\gamma$ branching ratio in the fiducial region $m_{\ell\ell} < 30$ GeV.

7 Systematic uncertainties

The total observed systematic uncertainty in the signal strength is 11%, which is about 35% the size of the statistical uncertainty. Therefore, systematic uncertainties play a subdominant role in this analysis.

The dominant experimental systematic uncertainties are due to the estimated biases in the fitted signal events (spurious signal, see Section 6). The corresponding uncertainty in the observed signal strength amounts to 6.1%. Other non-negligible systematic uncertainties relate to photon and lepton identification efficiencies in the simulated signal samples, in particular for merged-ee objects, as well as the energy/momentum calibration (see Section 4). Including jet uncertainties, which have a much smaller impact, these add up to 4.0%.

Furthermore, the luminosity uncertainty is taken into account, which is 1.7% in the combined 2015−2018 dataset [95, 96]. Uncertainties in the pile-up modelling contribute 1.7%. Uncertainties in the estimate of the $H \to \gamma\gamma$ background have a small impact, 0.7%. They include uncertainties in the photon-electron fake rate, and the uncertainties in the $\sigma(H) \times \mathcal{B}(H \to \gamma\gamma)$ measurement [93].

The assumed uncertainty in the $H \to \gamma^*\gamma \to \ell\ell\gamma$ branching ratio contributes 5.8%. The choice of the QCD scales impacts the number and distribution of signal events in the different categories and is evaluated for the ggF, VBF, and VH production modes using a scheme similar to the one discussed in Ref. [93]. The corresponding uncertainty in the measured signal strength is 4.7%. Uncertainties in the PDF are evaluated by using the eigenvectors of the PDF4LHC15 PDF set [33] and have a smaller effect of 2.3%. A conservative uncertainty of 50% is assigned on the normalization of the $t\bar{t}H$, $gg \to ZH$, and bbH production modes, as no dedicated $H \to \gamma^*\gamma \to \ell\ell\gamma$ samples are available, with an impact of 0.8%. Parton shower uncertainties contribute only 0.3%.

In the context of the $\sigma(H) \times \mathcal{B}(H \to \ell\ell\gamma)$ measurement, the effect of the theory uncertainties is reduced to 1.1% for the QCD scale and 0.9% for the PDF uncertainty, as only acceptance effects are considered, whereas the uncertainties in the predicted cross sections and branching ratio are removed.

8 Results

The $m_{\ell\ell\gamma}$ distributions of the selected events and the result of the global fit of the parametric signal-plus-background models to the data are shown in Figure 3 for each event category.

The best-fit value of the signal-strength parameter is $\mu = 1.5 \pm 0.5 = 1.5 \pm 0.5$ (stat.) $^{+0.2}_{-0.1}$ (syst.), while the corresponding expected value is $\mu_{\text{exp}} = 1.0 \pm 0.5 = 1.0 \pm 0.5$ (stat.) $^{+0.2}_{-0.1}$ (syst.). The best fit signal strength in the muon (electron) channel, obtained from a fit with two separate signal-strength parameters,

is $\mu_{\mu\mu} = 1.9 \pm 0.7$ ($\mu_{ee} = 1.0 \pm 0.7$). Figure 4 shows the results of the fit when the signal strength in each category is allowed to float independently. As expected, the low-$p_{\text{T}t}$ categories, especially in the $\mu\mu$ channel, have the smallest uncertainties (compare Table 1). It can be seen that all categories yield results that are consistent with each other and with the result of the single-μ fit.

Figure 5 shows the $m_{\ell\ell\gamma}$ distribution, with every data event reweighted by a category-dependent weight $\ln(1 + S_{90}/B_{90})$, where S_{90} is the number of signal events in the smallest window containing 90% of the expected signal and B_{90} is the expected number of background events in the same window, estimated from fits to the data sidebands using the background models.

The observed (expected) significance over the background-only hypothesis for a Higgs boson with a mass of 125.09 GeV is 3.2σ (2.1σ).

The Higgs boson production cross-section times the $H \rightarrow \ell\ell\gamma$ branching ratio for $m_{\ell\ell} < 30$ GeV is determined to be $8.7^{+2.8}_{-2.7}$ fb $= 8.7 \pm 2.7$ (stat.) $^{+0.7}_{-0.6}$ (syst.) fb.
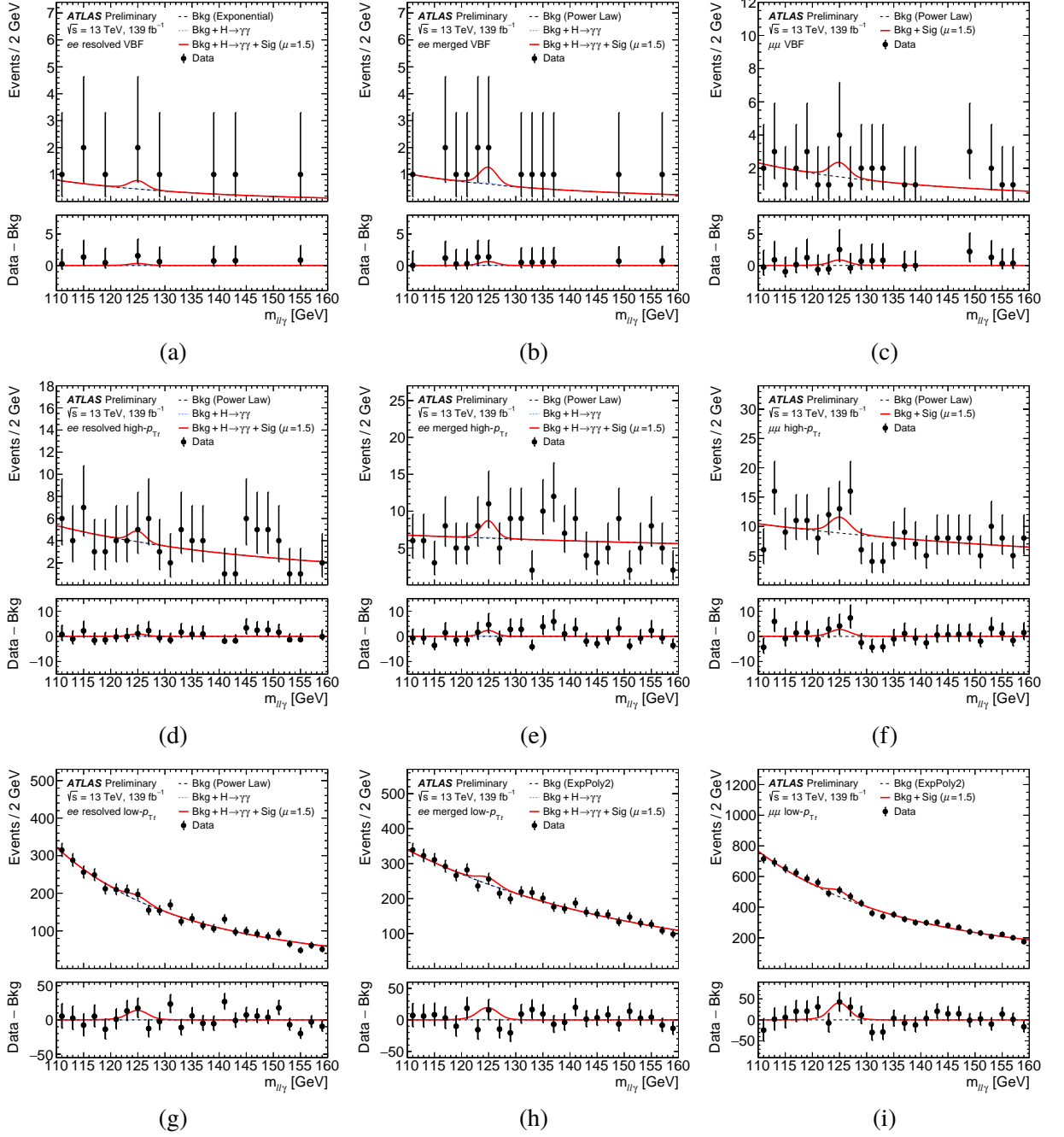
Figure 3: $m_{\ell\ell\gamma}$ distributions of the selected events and the results of the global fit, for the VBF-enriched categories (a, b, c), the high-p_{Tt} categories (d, e, f), and the low-p_{Tt} categories (g, h, i). The *ee*-resolved categories are shown in the left column, the *ee*-merged categories in the middle and the $\mu\mu$ categories in the right column. The data are shown as the black points with statistical uncertainties. The red curve shows the combined signal-plus-background model, the dashed black line shows the model of the non-resonant background component and the dotted blue line denotes the sum of the non-resonant background and the resonant $H \to \gamma\gamma$ background. The curves are obtained from the fit, i.e. they include the best-fit values of the parameter of interest and the nuisance parameters, including the spurious signal. The bottom panel shows the residuals of the data with respect to the non-resonant background component of the signal-plus-background fit.
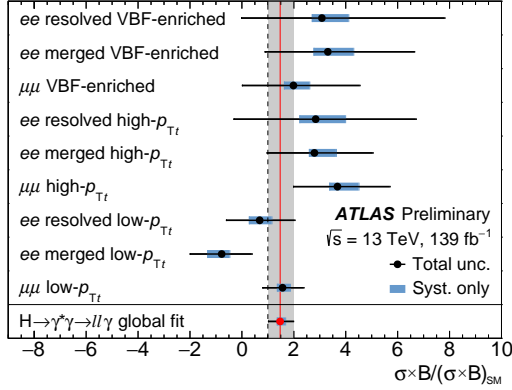
Figure 4: Best-fit values of the signal strength parameters for all event categories, in a fit where the signal strength in each category is allowed to float independently, compared with the result of the global fit.
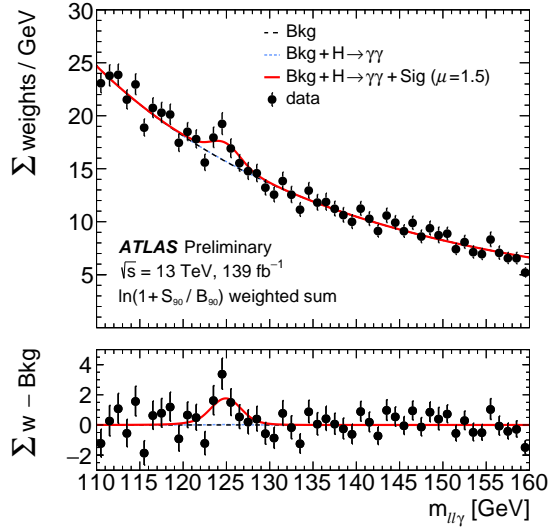

Figure 5: $m_{\ell\ell\gamma}$ distribution, with every data event reweighted by a category-dependent weight, $\ln\left(1 + S_{90}/B_{90}\right)$, where S_{90} is the number of signal events in the smallest window containing 90% of the expected signal, and B_{90} is the expected number of background events in the same window, estimated from fits to the data sidebands using the background models. The data are shown as the black points with statistical uncertainties. The parameterised signal and backgrounds are also added up with the category-dependent weight. The red curve shows the combined signal-plus-background model when fitting all analysis categories simultaneously, the dashed black line shows the model of the non-resonant background component and the dotted blue line denotes the sum of the non-resonant background and the resonant $H \to \gamma\gamma$ background. The curves are obtained from the fit, i.e. they include the best-fit values of the parameter of interest and the nuisance parameters, including the spurious signal. The bottom panel shows the residuals of the data with respect to the non-resonant background component of the signal-plus-background fit.

14

9 Conclusion

A search for the Higgs boson decaying into a low-mass pair of electrons or muons and a photon is presented. The analysis is performed using a data set recorded by the ATLAS experiment at the LHC with proton–proton collisions at a centre-of-mass energy of 13 TeV, corresponding to an integrated luminosity of 139 fb^{-1}. For a Higgs boson with a mass of 125.09 GeV and $m_{\ell\ell} < 30$ GeV, evidence for the $H \to \ell\ell\gamma$ process is found with a significance of 3.2σ over the background-only hypothesis, compared to an expected significance of 2.1σ. The best-fit value of the signal strength parameter, defined as the ratio of the observed signal yield to the one expected in the Standard Model, is $\mu = 1.5 \pm 0.5$. The Higgs boson production cross-section times the $H \to \ell\ell\gamma$ branching ratio for $m_{\ell\ell} < 30$ GeV is determined to be 8.7 $^{+2.8}_{-2.7}$ fb. This result constitutes the first evidence for the decay of the Higgs boson to a pair of leptons and a photon, an important step towards probing Higgs boson couplings in this rare decay channel.

References

[1] ATLAS Collaboration, *Observation of a new particle in the search for the Standard Model Higgs boson with the ATLAS detector at the LHC*, Phys. Lett. B **716** (2012) 1, arXiv: 1207.7214 [hep-ex] (cit. on pp. 2, 10).

[2] CMS Collaboration, *Observation of a new boson at a mass of 125 GeV with the CMS experiment at the LHC*, Phys. Lett. B **716** (2012) 30, arXiv: 1207.7235 [hep-ex] (cit. on p. 2).

[3] ATLAS Collaboration, *Study of the spin and parity of the Higgs boson in diboson decays with the ATLAS detector*, Eur. Phys. J. C **75** (2015) 476, arXiv: 1506.05669 [hep-ex] (cit. on p. 2), Erratum: Eur. Phys. J. C **76** (2016) 152.

[4] CMS Collaboration, *Constraints on the spin-parity and anomalous HVV couplings of the Higgs boson in proton collisions at 7 and 8 TeV*, Phys. Rev. D **92** (2015) 012004, arXiv: 1411.3441 [hep-ex] (cit. on p. 2).

[5] ATLAS and CMS Collaborations, *Measurements of the Higgs boson production and decay rates and constraints on its couplings from a combined ATLAS and CMS analysis of the LHC pp collision data at $\sqrt{s} = 7$ and 8 TeV*, JHEP **08** (2016) 045, arXiv: 1606.02266 [hep-ex] (cit. on p. 2).

[6] CMS Collaboration, *Combined measurements of Higgs boson couplings in proton–proton collisions at $\sqrt{s} = 13$ TeV*, Eur. Phys. J. C **79** (2019) 421, arXiv: 1809.10733 [hep-ex] (cit. on p. 2).

[7] ATLAS Collaboration, *Combined measurements of Higgs boson production and decay using up to 80 fb^{-1} of proton–proton collision data at $\sqrt{s} = 13$ TeV collected with the ATLAS experiment*, Phys. Rev. D **101** (2020) 012002, arXiv: 1909.02845 [hep-ex] (cit. on p. 2).

[8] A. Kachanovich, U. Nierste and I. Nišandžić, *Higgs boson decay into a lepton pair and a photon revisited*, Phys. Rev. D **101** (2020) 073003, arXiv: 2001.06516 [hep-ph] (cit. on pp. 2, 4).

[9] A. Y. Korchin and V. A. Kovalchuk, *Angular distribution and forward–backward asymmetry of the Higgs-boson decay to photon and lepton pair*, Eur. Phys. J. C **74** (2014) 3141, arXiv: 1408.0342 [hep-ph] (cit. on p. 2).

[10] Y. Chen, A. Falkowski, I. Low and R. Vega-Morales, *New Observables for CP Violation in Higgs Decays*, Phys. Rev. D **90** (2014) 113006, arXiv: 1405.6723 [hep-ph] (cit. on p. 2).

[11] L.-B. Chen, C.-F. Qiao and R.-L. Zhu, *Reconstructing the 125 GeV SM Higgs Boson Through $\ell\bar{\ell}\gamma$*, Phys. Lett. B **726** (2013) 306, Erratum: Phys. Lett. B **808** (2020) 135629, arXiv: 1211.6058 [hep-ph] (cit. on pp. 2, 4).

[12] G. Passarino, *Higgs Boson Production and Decay: Dalitz Sector*, Phys. Lett. B **727** (2013) 424, arXiv: 1308.0422 [hep-ph] (cit. on pp. 2, 4, 5).

[13] CMS Collaboration, *Search for the decay of a Higgs boson in the $\ell\ell\gamma$ channel in proton-proton collisions at $\sqrt{s}$ = 13 TeV*, JHEP **11** (2018) 152, arXiv: 1806.05996 [hep-ex] (cit. on p. 2).

[14] ATLAS Collaboration, *A search for the $Z\gamma$ decay mode of the Higgs boson in pp collisions at $\sqrt{s}$ = 13 TeV with the ATLAS detector*, Phys. Lett. B **809** (2020) 135754, arXiv: 2005.05382 [hep-ex] (cit. on p. 2).

[15] CMS Collaboration, *Search for a Higgs boson decaying into $\gamma^*\gamma \to \ell\ell\gamma$ with low dilepton mass in pp collisions at $\sqrt{s}$ = 8 TeV*, Phys. Lett. B **753** (2016) 341, arXiv: 1507.03031 [hep-ex] (cit. on p. 2).

[16] ATLAS Collaboration, *The ATLAS Experiment at the CERN Large Hadron Collider*, JINST **3** (2008) S08003 (cit. on p. 3).

[17] ATLAS Collaboration, *ATLAS Insertable B-Layer Technical Design Report*, ATLAS-TDR-19 (2010), URL: https://cds.cern.ch/record/1291633, *ATLAS Insertable B-Layer Technical Design Report Addendum*, ATLAS-TDR-19-ADD-1, 2012, URL: https://cds.cern.ch/record/1451888 (cit. on p. 3).

[18] B. Abbott et al., *Production and integration of the ATLAS Insertable B-Layer*, JINST **13** (2018) T05008, arXiv: 1803.00844 [physics.ins-det] (cit. on p. 3).

[19] ATLAS Collaboration, *Electron and photon performance measurements with the ATLAS detector using the 2015–2017 LHC proton–proton collision data*, JINST **14** (2019) P12006, arXiv: 1908.00005 [hep-ex] (cit. on pp. 3, 5, 6).

[20] ATLAS Collaboration, *Performance of the ATLAS trigger system in 2015*, Eur. Phys. J. C **77** (2017) 317, arXiv: 1611.09661 [hep-ex] (cit. on p. 3).

[21] ATLAS Collaboration, *ATLAS data quality operations and performance for 2015–2018 data-taking*, JINST **15** (2020) P04003, arXiv: 1911.04632 [physics.ins-det] (cit. on p. 3).

[22] ATLAS Collaboration, *Performance of electron and photon triggers in ATLAS during LHC Run 2*, Eur. Phys. J. C **80** (2020) 47, arXiv: 1909.00761 [hep-ex] (cit. on p. 3).

[23] ATLAS Collaboration, *The ATLAS simulation infrastructure*, Eur. Phys. J. C **70** (2010) 823, arXiv: 1005.4568 [physics.ins-det] (cit. on p. 4).

[24] S. Agostinelli et al., *GEANT4 - a simulation toolkit*, Nucl. Instrum. Methods A **506** (2003) 250 (cit. on p. 4).

[25] T. Sjöstrand, S. Mrenna and P. Skands, *A brief introduction to PYTHIA 8.1*,
Comput. Phys. Commun. **178** (2008) 852, arXiv: 0710.3820 [hep-ph] (cit. on p. 4).

[26] R. D. Ball et al., *Parton distributions with LHC data*, Nucl. Phys. B **867** (2013) 244,
arXiv: 1207.1303 [hep-ph] (cit. on p. 4).

[27] ATLAS Collaboration, *The Pythia 8 A3 tune description of ATLAS minimum bias and inelastic measurements incorporating the Donnachie–Landshoff diffractive model*,
ATL-PHYS-PUB-2016-017, 2016, URL: https://cds.cern.ch/record/2206965 (cit. on p. 4).

[28] P. Nason and C. Oleari,
NLO Higgs boson production via vector-boson fusion matched with shower in POWHEG,
JHEP **02** (2010) 037, arXiv: 0911.5299 [hep-ph] (cit. on p. 4).

[29] S. Alioli, P. Nason, C. Oleari and E. Re, *A general framework for implementing NLO calculations in shower Monte Carlo programs: the POWHEG BOX*, JHEP **06** (2010) 043, (using ATLAS svn revisions r2856 for v1, r3080 for v2 ggF, r3052 for v2 VBF, and r3133 for v2 *VH*),
arXiv: 1002.2581 [hep-ph] (cit. on p. 4).

[30] P. Nason, *A new method for combining NLO QCD with shower Monte Carlo algorithms*,
JHEP **11** (2004) 040, arXiv: hep-ph/0409146 (cit. on p. 4).

[31] S. Frixione, P. Nason and C. Oleari,
Matching NLO QCD computations with Parton Shower simulations: the POWHEG method,
JHEP **11** (2007) 070, arXiv: 0709.2092 [hep-ph] (cit. on p. 4).

[32] H. B. Hartanto, B. Jager, L. Reina and D. Wackeroth,
Higgs boson production in association with top quarks in the POWHEG BOX,
Phys. Rev. D **91** (2015) 094003, arXiv: 1501.04498 [hep-ph] (cit. on p. 4).

[33] J. Butterworth et al., *PDF4LHC recommendations for LHC Run II*, J. Phys G **43** (2016) 023001,
arXiv: 1510.03865 [hep-ph] (cit. on pp. 4, 11).

[34] K. Hamilton, P. Nason, E. Re and G. Zanderighi, *NNLOPS simulation of Higgs boson production*,
JHEP **10** (2013) 222, arXiv: 1309.0017 [hep-ph] (cit. on p. 4).

[35] K. Hamilton, P. Nason and G. Zanderighi,
Finite quark-mass effects in the NNLOPS POWHEG+MiNLO Higgs generator,
JHEP **05** (2015) 140, arXiv: 1501.04637 [hep-ph] (cit. on p. 4).

[36] S. Catani and M. Grazzini, *An NNLO subtraction formalism in hadron collisions and its application to Higgs boson production at the LHC*, Phys. Rev. Lett. **98** (2007) 222002,
arXiv: hep-ph/0703012 [hep-ph] (cit. on p. 4).

[37] G. Cullen et al., *Automated One-Loop Calculations with GoSam*, Eur. Phys. J. C **72** (2012) 1889,
arXiv: 1111.2034 [hep-ph] (cit. on p. 4).

[38] K. Hamilton, P. Nason, C. Oleari and G. Zanderighi, *Merging H/W/Z + 0 and 1 jet at NLO with no merging scale: a path to parton shower + NNLO matching*, JHEP **05** (2013) 082,
arXiv: 1212.4504 [hep-ph] (cit. on p. 4).

[39] G. Luisoni, P. Nason, C. Oleari and F. Tramontano, *HW$^\pm$/HZ + 0 and 1 jet at NLO with the POWHEG BOX interfaced to GoSam and their merging within MiNLO*, JHEP **10** (2013) 083,
arXiv: 1306.2542 [hep-ph] (cit. on p. 4).

[40] J. Bellm et al., *Herwig 7.0/Herwig++ 3.0 release note*, Eur. Phys. J. C **76** (2016) 196,
arXiv: 1512.01178 [hep-ph] (cit. on p. 4).

[41] D. de Florian et al.,
Handbook of LHC Higgs Cross Sections: 4. Deciphering the Nature of the Higgs Sector, (2016),
arXiv: 1610.07922 [hep-ph] (cit. on pp. 4, 5).

[42] ATLAS and CMS Collaborations, *Combined Measurement of the Higgs Boson Mass in pp
Collisions at $\sqrt{s}$ = 7 and 8 TeV with the ATLAS and CMS Experiments*,
Phys. Rev. Lett. **114** (2015) 191803, arXiv: 1503.07589 [hep-ex] (cit. on pp. 4, 10).

[43] C. Anastasiou, C. Duhr, F. Dulat, F. Herzog and B. Mistlberger,
Higgs Boson Gluon-Fusion Production in QCD at Three Loops, Phys. Rev. Lett. **114** (2015) 212001,
arXiv: 1503.06056 [hep-ph] (cit. on p. 4).

[44] C. Anastasiou et al.,
High precision determination of the gluon fusion Higgs boson cross-section at the LHC,
JHEP **05** (2016) 058, arXiv: 1602.00695 [hep-ph] (cit. on p. 4).

[45] F. Dulat, A. Lazopoulos and B. Mistlberger, *iHixs 2 – Inclusive Higgs cross sections*,
Comput. Phys. Commun. **233** (2018) 243, arXiv: 1802.00827 [hep-ph] (cit. on p. 4).

[46] R. V. Harlander and K. J. Ozeren,
Finite top mass effects for hadronic Higgs production at next-to-next-to-leading order,
JHEP **11** (2009) 088, arXiv: 0909.3420 [hep-ph] (cit. on p. 4).

[47] R. V. Harlander and K. J. Ozeren,
Top mass effects in Higgs production at next-to-next-to-leading order QCD: Virtual corrections,
Phys. Lett. B **679** (2009) 467, arXiv: 0907.2997 [hep-ph] (cit. on p. 4).

[48] R. V. Harlander, H. Mantler, S. Marzani and K. J. Ozeren,
Higgs production in gluon fusion at next-to-next-to-leading order QCD for finite top mass,
Eur. Phys. J. C **66** (2010) 359, arXiv: 0912.2104 [hep-ph] (cit. on p. 4).

[49] A. Pak, M. Rogal and M. Steinhauser,
Finite top quark mass effects in NNLO Higgs boson production at LHC, JHEP **02** (2010) 025,
arXiv: 0911.4662 [hep-ph] (cit. on p. 4).

[50] S. Actis, G. Passarino, C. Sturm and S. Uccirati,
NLO electroweak corrections to Higgs boson production at hadron colliders,
Phys. Lett. B **670** (2008) 12, arXiv: 0809.1301 [hep-ph] (cit. on p. 4).

[51] S. Actis, G. Passarino, C. Sturm and S. Uccirati,
NNLO computational techniques: The cases $H \to \gamma\gamma$ and $H \to gg$, Nucl. Phys. B **811** (2009) 182,
arXiv: 0809.3667 [hep-ph] (cit. on p. 4).

[52] C. Anastasiou, R. Boughezal and F. Petriello,
Mixed QCD-electroweak corrections to Higgs boson production in gluon fusion,
JHEP **04** (2009) 003, arXiv: 0811.3458 [hep-ph] (cit. on p. 4).

[53] U. Aglietti, R. Bonciani, G. Degrassi and A. Vicini,
Two loop light fermion contribution to Higgs production and decays, Phys. Lett. B **595** (2004) 432,
arXiv: hep-ph/0404071 [hep-ph] (cit. on p. 4).

[54] M. Bonetti, K. Melnikov and L. Tancredi, *Higher order corrections to mixed QCD-EW
contributions to Higgs boson production in gluon fusion*,
Phys. Rev. D **97** (2018) 056017, Erratum: Phys. Rev. D **97** (2018) 099906,
arXiv: 1801.10403 [hep-ph] (cit. on p. 4).

[55] M. Ciccolini, A. Denner and S. Dittmaier, *Strong and electroweak corrections to the production of Higgs+2jets via weak interactions at the LHC*, Phys. Rev. Lett. **99** (2007) 161803, arXiv: 0707.0381 [hep-ph] (cit. on p. 4).

[56] M. Ciccolini, A. Denner and S. Dittmaier, *Electroweak and QCD corrections to Higgs production via vector-boson fusion at the LHC*, Phys. Rev. D **77** (2008) 013002, arXiv: 0710.4749 [hep-ph] (cit. on p. 4).

[57] P. Bolzoni, F. Maltoni, S.-O. Moch and M. Zaro, *Higgs Boson Production via Vector-Boson Fusion at Next-to-Next-to-Leading Order in QCD*, Phys. Rev. Lett. **105** (2010) 011801, arXiv: 1003.4451 [hep-ph] (cit. on p. 4).

[58] M. L. Ciccolini, S. Dittmaier and M. Krämer, *Electroweak radiative corrections to associated WH and ZH production at hadron colliders*, Phys. Rev. D **68** (2003) 073003, arXiv: hep-ph/0306234 [hep-ph] (cit. on p. 4).

[59] O. Brein, A. Djouadi and R. Harlander, *NNLO QCD corrections to the Higgs-strahlung processes at hadron colliders*, Phys. Lett. B **579** (2004) 149, arXiv: hep-ph/0307206 (cit. on p. 4).

[60] O. Brein, R. Harlander, M. Wiesemann and T. Zirke, *Top-Quark Mediated Effects in Hadronic Higgs-Strahlung*, Eur. Phys. J. C **72** (2012) 1868, arXiv: 1111.0761 [hep-ph] (cit. on p. 4).

[61] L. Altenkamp, S. Dittmaier, R. V. Harlander, H. Rzehak and T. J. E. Zirke, *Gluon-induced Higgs-strahlung at next-to-leading order QCD*, JHEP **02** (2013) 078, arXiv: 1211.5015 [hep-ph] (cit. on p. 4).

[62] A. Denner, S. Dittmaier, S. Kallweit and A. Mück, *HAWK 2.0: A Monte Carlo program for Higgs production in vector-boson fusion and Higgs strahlung at hadron colliders*, Comput. Phys. Commun. **195** (2015) 161, arXiv: 1412.5390 [hep-ph] (cit. on p. 4).

[63] O. Brein, R. V. Harlander and T. J. E. Zirke, *vh@nnlo – Higgs Strahlung at hadron colliders*, Comput. Phys. Commun. **184** (2013) 998, arXiv: 1210.5347 [hep-ph] (cit. on p. 4).

[64] R. V. Harlander, A. Kulesza, V. Theeuwes and T. Zirke, *Soft gluon resummation for gluon-induced Higgs Strahlung*, JHEP **11** (2014) 082, arXiv: 1410.0217 [hep-ph] (cit. on p. 4).

[65] R. V. Harlander, J. Klappert, S. Liebler and L. Simon, *vh@nnlo-v2: New physics in Higgs Strahlung*, JHEP **05** (2018) 089, arXiv: 1802.04817 [hep-ph] (cit. on p. 4).

[66] W. Beenakker et al., *NLO QCD corrections to t̄tH production in hadron collisions*, Nucl. Phys. B **653** (2003) 151, arXiv: hep-ph/0211352 (cit. on p. 4).

[67] S. Dawson, C. Jackson, L. H. Orr, L. Reina and D. Wackeroth, *Associated Higgs boson production with top quarks at the CERN Large Hadron Collider: NLO QCD corrections*, Phys. Rev. D **68** (2003) 034022, arXiv: hep-ph/0305087 (cit. on p. 4).

[68] Y. Zhang, W.-G. Ma, R.-Y. Zhang, C. Chen and L. Guo, *QCD NLO and EW NLO corrections to t̄tH production with top quark decays at hadron collider*, Phys. Lett. B **738** (2014) 1, arXiv: 1407.1110 [hep-ph] (cit. on p. 4).

[69] S. Frixione, V. Hirschi, D. Pagani, H.-S. Shao and M. Zaro, *Electroweak and QCD corrections to top-pair hadroproduction in association with heavy bosons*, JHEP **06** (2015) 184, arXiv: 1504.03446 [hep-ph] (cit. on p. 4).

19

[70] S. Dawson, C. Jackson, L. Reina and D. Wackeroth,
Exclusive Higgs boson production with bottom quarks at hadron colliders,
Phys. Rev. D **69** (2004) 074027, arXiv: `hep-ph/0311067` (cit. on p. 4).

[71] S. Dittmaier, M. Krämer and M. Spira,
Higgs radiation off bottom quarks at the Tevatron and the CERN LHC,
Phys. Rev. D **70** (2004) 074010, arXiv: `hep-ph/0309204` (cit. on p. 4).

[72] R. Harlander, M. Kramer and M. Schumacher, *Bottom-quark associated Higgs-boson production: reconciling the four- and five-flavour scheme approach*, (2011), arXiv: `1112.3478 [hep-ph]`
(cit. on p. 4).

[73] A. Abbasabadi, D. Bowser-Chao, D. A. Dicus and W. W. Repko,
Radiative Higgs boson decays $H \to f\bar{f}\gamma$, Phys. Rev. D **55** (1997) 5647, arXiv: `hep-ph/9611209`
(cit. on p. 4).

[74] A. Firan and R. Stroynowski, *Internal conversions in Higgs decays to two photons*,
Phys. Rev. D **76** (2007) 057301, arXiv: `0704.3987 [hep-ph]` (cit. on p. 4).

[75] D. A. Dicus and W. W. Repko, *Calculation of the decay $H \to e\bar{e}\gamma$*, Phys. Rev. D **87** (2013) 077301,
arXiv: `1302.2159 [hep-ph]` (cit. on p. 4).

[76] D. A. Dicus and W. W. Repko, *Dalitz decay $H \to f\bar{f}\gamma$ as a background for $H \to \gamma\gamma$*,
Phys. Rev. D **89** (2014) 093013, arXiv: `1402.5317 [hep-ph]` (cit. on p. 4).

[77] E. Bothmann et al., *Event Generation with Sherpa 2.2*, SciPost Phys. **7** (2019) 034,
arXiv: `1905.09127 [hep-ph]` (cit. on p. 5).

[78] R. D. Ball et al., *Parton distributions for the LHC Run II*, JHEP **04** (2015) 040,
arXiv: `1410.8849 [hep-ph]` (cit. on p. 5).

[79] ATLAS Collaboration, *Muon reconstruction performance of the ATLAS detector in proton–proton collision data at $\sqrt{s}$ = 13 TeV*, Eur. Phys. J. C **76** (2016) 292, arXiv: `1603.05598 [hep-ex]`
(cit. on p. 5).

[80] ATLAS Collaboration, *Muon reconstruction and identification efficiency in ATLAS using the full Run 2 pp collision data set at $\sqrt{s}$ = 13 TeV*, (2020), arXiv: `2012.00578 [hep-ex]` (cit. on p. 5).

[81] ATLAS Collaboration, *Measurement of the photon identification efficiencies with the ATLAS detector using LHC Run 2 data collected in 2015 and 2016*, Eur. Phys. J. C **79** (2019) 205,
arXiv: `1810.05087 [hep-ex]` (cit. on pp. 5, 6).

[82] ATLAS Collaboration, *Electron reconstruction and identification in the ATLAS experiment using the 2015 and 2016 LHC proton–proton collision data at $\sqrt{s}$ = 13 TeV*, Eur. Phys. J. C **79** (2019) 639,
arXiv: `1902.04655 [hep-ex]` (cit. on p. 6).

[83] R. Fruhwirth, *Application of Kalman filtering to track and vertex fitting*,
Nucl. Instrum. Meth. A **262** (1987) 444 (cit. on p. 6).

[84] ATLAS Collaboration,
Particle Identification Performance of the ATLAS Transition Radiation Tracker,
ATLAS-CONF-2011-128, 2011, URL: `https://cds.cern.ch/record/1383793` (cit. on p. 6).

[85] ATLAS Collaboration,
Topological cell clustering in the ATLAS calorimeters and its performance in LHC Run 1,
Eur. Phys. J. C **77** (2017) 490, arXiv: `1603.02934 [hep-ex]` (cit. on p. 7).

[86] M. Cacciari, G. P. Salam and G. Soyez, *The anti-k_t jet clustering algorithm*, JHEP **04** (2008) 063, arXiv: `0802.1189 [hep-ph]` (cit. on p. 7).

[87] ATLAS Collaboration, *Tagging and suppression of pileup jets with the ATLAS detector*, ATLAS-CONF-2014-018 (2014), URL: `https://cds.cern.ch/record/1700870` (cit. on p. 7).

[88] D. L. Rainwater, R. Szalapski and D. Zeppenfeld, *Probing color singlet exchange in Z + two jet events at the CERN LHC*, Phys. Rev. D **54** (1996) 6680, arXiv: `hep-ph/9605444` (cit. on p. 8).

[89] OPAL Collaboration, K. Ackerstaff et al., *Search for anomalous production of dilepton events with missing transverse momentum in e^+e^- collisions at $\sqrt{s}$ = 161 GeV and 172 GeV*, Eur. Phys. J. C **4** (1998) 47, arXiv: `hep-ex/9710010` (cit. on p. 8).

[90] M. Vesterinen and T. Wyatt, *A novel technique for studying the Z boson transverse momentum distribution at hadron colliders*, Nucl. Instrum. Meth. A **602** (2009) 432, arXiv: `0807.4956 [hep-ph]` (cit. on p. 8).

[91] M. Oreglia, *A Study of the Reactions $\psi' \to \gamma\gamma\psi$*, 1980, URL: `https://www.slac.stanford.edu/cgi-wrap/getdoc/slac-r-236.pdf` (cit. on p. 9).

[92] ATLAS Collaboration, *Search for Scalar Diphoton Resonances in the Mass Range 65-600 GeV with the ATLAS Detector in pp Collision Data at $\sqrt{s}$ = 8 TeV*, Phys. Rev. Lett. **113** (2014) 171801, arXiv: `1407.6583 [hep-ex]` (cit. on p. 9).

[93] ATLAS Collaboration, *Measurements of Higgs boson properties in the diphoton decay channel with $36\,fb^{-1}$ of pp collision data at $\sqrt{s}$ = 13 TeV with the ATLAS detector*, Phys. Rev. D **98** (2018) 052005, arXiv: `1802.04146 [hep-ex]` (cit. on pp. 10, 11).

[94] G. Cowan, K. Cranmer, E. Gross and O. Vitells, *Asymptotic formulae for likelihood-based tests of new physics*, Eur. Phys. J. C **71** (2011) 1554, arXiv: `1007.1727 [physics.data-an]`, Erratum: Eur. Phys. J. C **73** (2013) 2501 (cit. on p. 11).

[95] ATLAS Collaboration, *Luminosity determination in pp collisions at $\sqrt{s}$ = 13 TeV using the ATLAS detector at the LHC*, ATLAS-CONF-2019-021, 2019, URL: `https://cds.cern.ch/record/2677054` (cit. on p. 11).

[96] G. Avoni et al., *The new LUCID-2 detector for luminosity measurement and monitoring in ATLAS*, JINST **13** (2018) P07017 (cit. on p. 11).
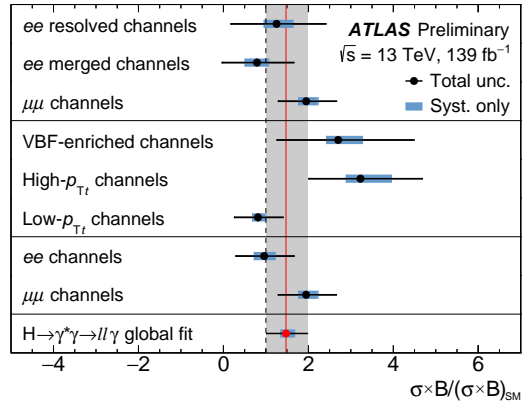
Appendix

Figure 6: Best-fit values of the signal strength parameters, in different fits with common signal strength parameters defined per event category or lepton flavour. In the first fit, there is a common signal signal strength for all *ee*-resolved categories, a separate one for all *ee*-merged categories, and one for all $\mu\mu$ categories. In the second fit, there are three independent signal strenth parameters for VBF-enriched, high-p_{Tt}, and low-p_{Tt} categories. In the final fit, there are two signal strength parameters, one shared by all *ee* categories and one for all $\mu\mu$ categories. These results are compared with the result of the global fit.
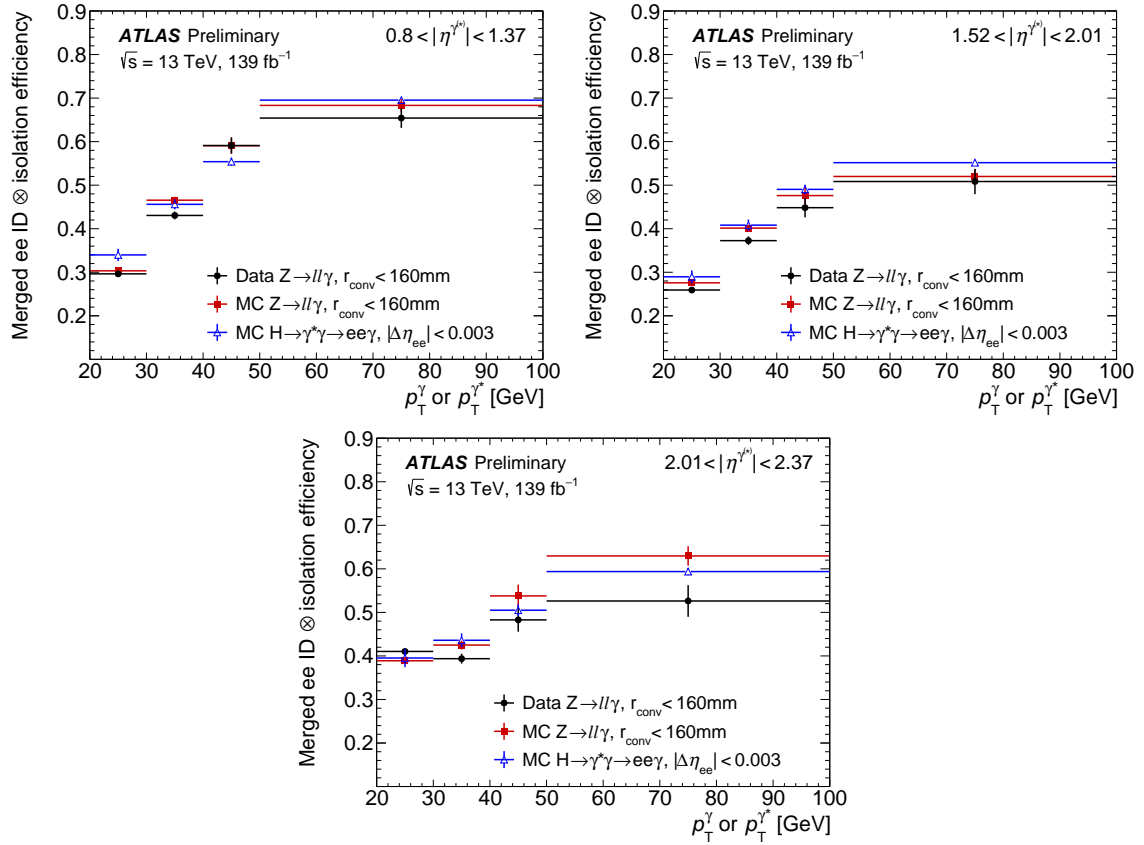
Figure 7: Combined merged-*ee* identification and isolation efficiency extracted from $Z \rightarrow \ell\ell\gamma$ events with a converted photon with $r_{\mathrm{conv}} < 160$ mm as a function of merged-*ee* p_{T} in the (top-left) $0.8 < |\eta| < 1.37$, (top-right) $1.52 < |\eta| < 2.01$ and (bottom) $2.01 < |\eta| < 2.37$ range. Data efficiencies (black points) are compared with efficiencies in simulated $Z \rightarrow \ell\ell\gamma$ events (blue markers). Additionally, the results are compared with those in simulated $H \rightarrow \gamma^*\gamma \rightarrow ee\gamma$ events.
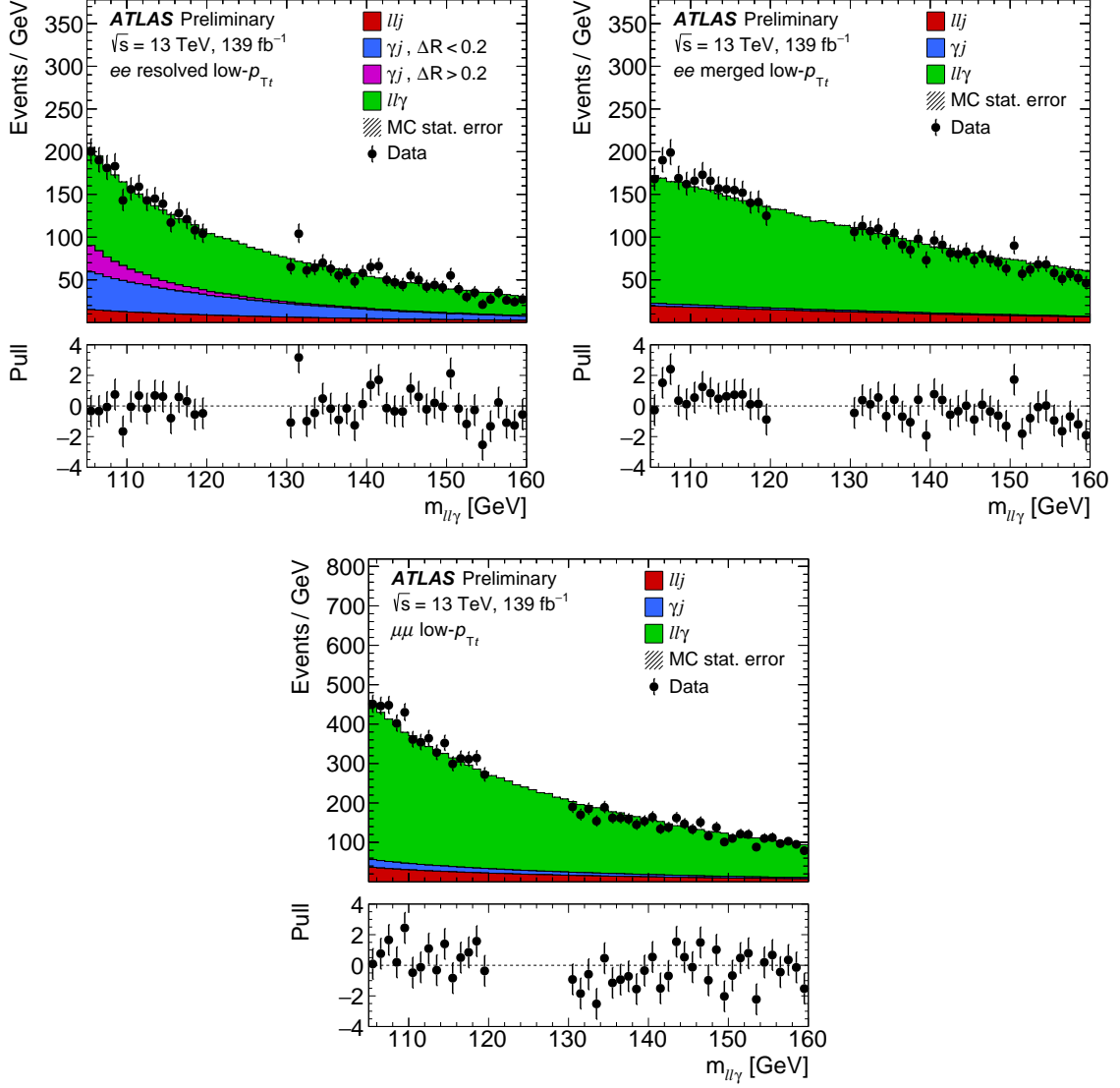
Figure 8: $m_{\ell\ell\gamma}$ distributions for events satisfying the $H \to \gamma^*\gamma \to \ell\ell\gamma$ selection in data for several event categories: (top-left) ee resolved low-$p_{\mathrm{T}t}$, (top-right) ee merged low-$p_{\mathrm{T}t}$, and (bottom) $\mu\mu$ low-$p_{\mathrm{T}t}$. The black points show the data with error bars for the statistical uncertainty. The contribution from non-resonant $\ell\ell\gamma$ process (green, obtained from simulation), and the contributions from the $\ell\ell$+jets and γ+jets processes (red and blue/purple, obtained from data control regions) are shown as stacked histograms; the total background estimate is normalised to the number of data events. Two γ+jets populations with different fake rates and mass distributions are found in the categories involving resolved electrons, separated according to the angular distance between the electrons ΔR. The bottom panels show the normalised residuals (pulls) of the data with respect to the sum of background components.
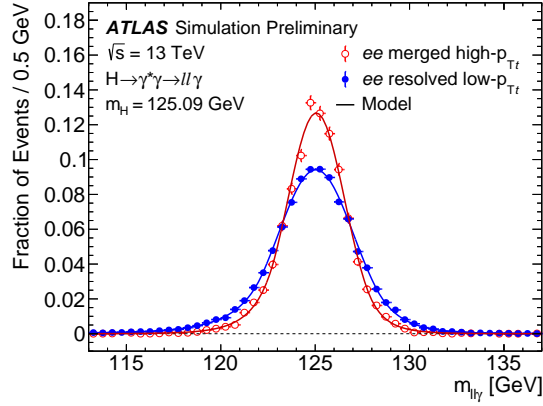
Figure 9: Simulated $m_{\ell\ell\gamma}$ invariant mass distribution for m_H = 125.09 GeV in the *ee*-merged high-p_{Tt} (red open circles) and *ee*-resolved low-p_{Tt} (blue closed circles) categories. Of the nine considered categories, the *ee*-merged high-p_{Tt} category has the best resolution, and the *ee*-resolved low-p_{Tt} category the worst. The parameterised signal models, obtained by fits with a Double-Sided Crystal-Ball function, are also shown.
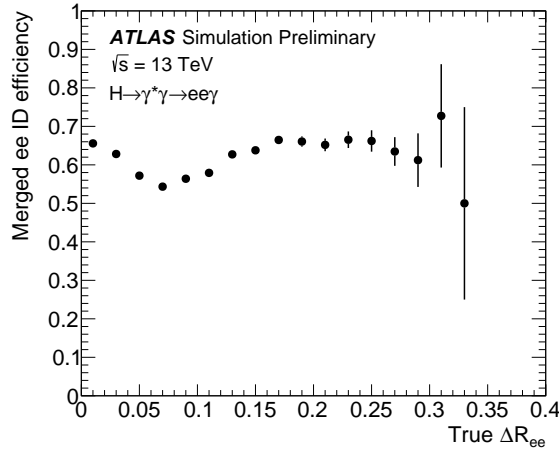

Figure 10: Merged-*ee* identification efficiency as a function of the true ΔR between the electrons (ΔR_{ee}) for simulated $H \rightarrow \gamma^*\gamma \rightarrow ee\gamma$ events. The denominator of the efficiency includes objects with an EM cluster matched to two opposite-charge tracks, each having $p_T > 5$ GeV, $|\eta| < 2.5$ and at least seven hits in the pixel and microstrip detectors combined. These preselected merged-*ee* objects are also required to have $p_T > 20$ GeV and $|\eta| < 2.37$. In addition, only events where both merged-*ee* tracks are matched to a generator-level electron from the $\gamma^* \rightarrow ee$ process are considered. Approximately 80% of events in the denominator are in the region $\Delta R_{ee} < 0.1$, where the standard electron identification algorithms are less efficient. The error bars represent the statistical uncertainty.
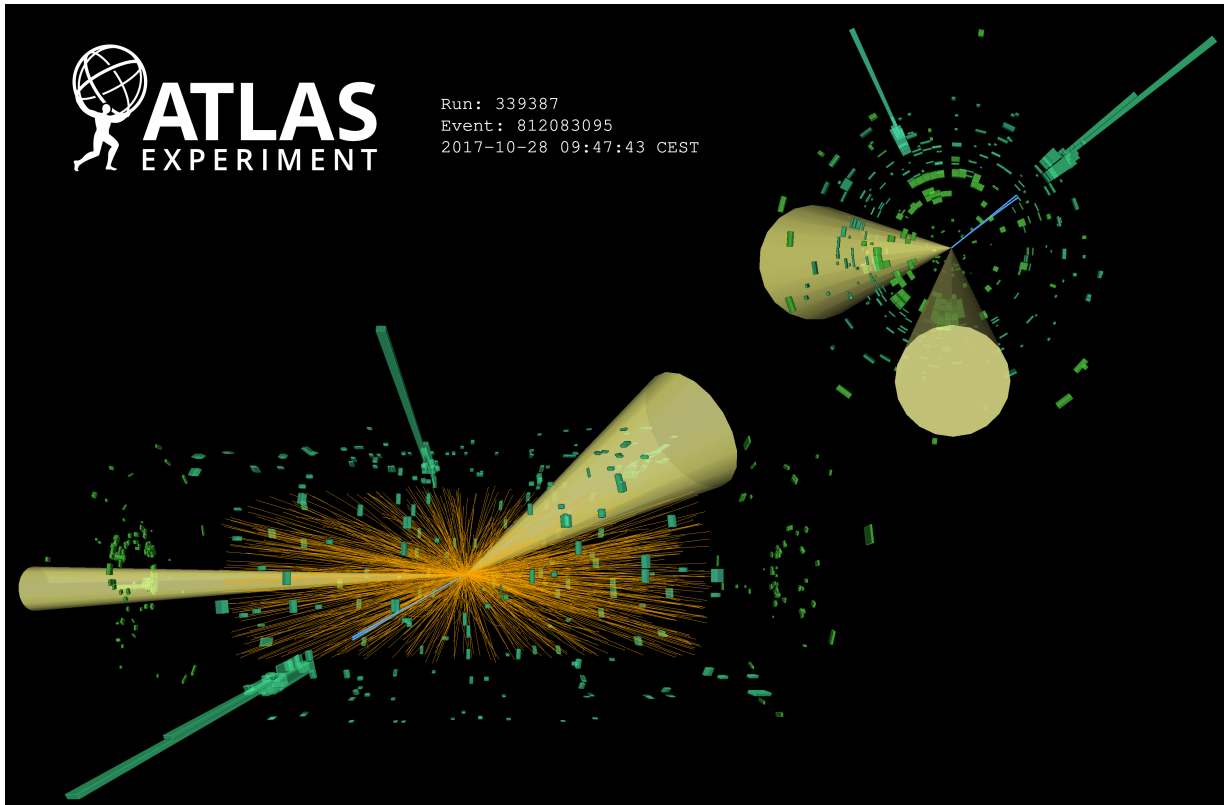
Figure 11: Event display of a candidate $H \rightarrow ee\gamma$ event from the *ee*-merged VBF-enriched category. The invariant mass of the *ee* system is 0.05 GeV and the invariant mass of the *eeγ* system is 125.8 GeV. The p_T of the photon is 72 GeV and the p_T of the merged-*ee* candidate is 103 GeV. The two visible jets have p_T^{j1} = 124 GeV and p_T^{j2} = 64 GeV, respectively, and m_{jj} = 664 GeV and $|\Delta\eta_{jj}|$ = 4.0.
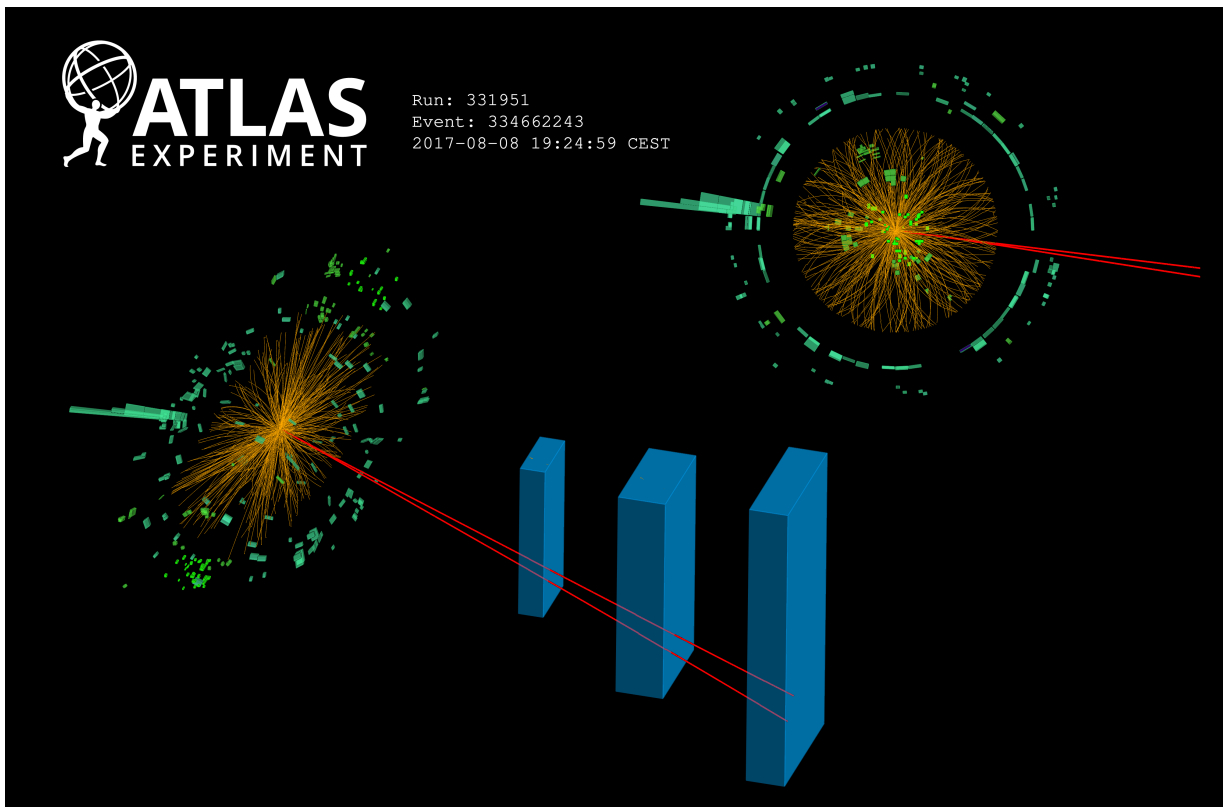
Figure 12: Event display of a candidate $H \to \mu\mu\gamma$ event from the $\mu\mu$ low-$p_{\mathrm{T}t}$ category. The invariant mass of the $\mu\mu$ system is 0.6 GeV and the invariant mass of the $\mu\mu\gamma$ system is 124.9 GeV. The p_{T} of the photon is 60 GeV, the p_{T} of the leading muon is 60 GeV and the p_{T} of the subleading muon is 28 GeV.

Table 2: Best-fit values of the signal strength parameters, in different fits with common signal strength parameters defined per event category or lepton flavour. In the first fit, there is a common signal strength for all *ee* resolved categories, a separate one for all *ee* merged categories, and one for all $\mu\mu$ categories. In the second fit, there are three independent signal strength parameters for VBF-enriched, high-$p_{\mathrm{T}t}$, and low-$p_{\mathrm{T}t}$ categories. In the final fit, there are two signal strength parameters, one shared by all *ee* categories and one for all $\mu\mu$ categories. These results are compared with the result of the global fit.

Category	Measured $(\sigma{\cdot}B)/(\sigma{\cdot}B)_{\mathrm{SM}}$	Uncertainty Total	(Stat.	Syst.)
ee resolved categories	1.3	$^{+1.2}_{-1.1}$	($^{+1.1}_{-1.0}$	$^{+0.4}_{-0.3}$)
ee merged categories	0.8	$^{+0.9}_{-0.8}$	(±0.8	±0.3)
$\mu\mu$ categories	1.9	±0.7	($^{+0.7}_{-0.6}$	$^{+0.3}_{-0.2}$)
VBF-enriched categories	2.7	$^{+1.8}_{-1.4}$	($^{+1.7}_{-1.4}$	$^{+0.6}_{-0.3}$)
high-$p_{\mathrm{T}t}$ categories	3.2	$^{+1.4}_{-1.2}$	($^{+1.3}_{-1.2}$	$^{+0.7}_{-0.3}$)
low-$p_{\mathrm{T}t}$ categories	0.8	±0.6	($^{+0.6}_{-0.5}$	$^{+0.2}_{-0.1}$)
ee categories	1.0	±0.7	($^{+0.7}_{-0.6}$	$^{+0.3}_{-0.2}$)
$\mu\mu$ categories	1.9	±0.7	($^{+0.7}_{-0.6}$	$^{+0.3}_{-0.2}$)
$H \rightarrow \gamma^*\gamma \rightarrow \ell\ell\gamma$ global fit	1.5	±0.5	(±0.5	$^{+0.2}_{-0.1}$)

Table 3: Best-fit values of the signal strength parameters for all event categories, in a fit where the signal strength in each category is allowed to float independently, compared with the result of the global fit.

Category	Measured $(\sigma{\cdot}B)/(\sigma{\cdot}B)_{\mathrm{SM}}$	Uncertainty Total	(Stat.	Syst.)
ee resolved VBF-enriched	3.1	$^{+4.7}_{-3.1}$	($^{+4.6}_{-3.1}$	$^{+1.0}_{-0.4}$)
ee merged VBF-enriched	3.3	$^{+3.3}_{-2.4}$	($^{+3.2}_{-2.4}$	$^{+1.0}_{-0.6}$)
$\mu\mu$ VBF-enriched	2.0	$^{+2.5}_{-2.0}$	($^{+2.5}_{-1.9}$	$^{+0.6}_{-0.4}$)
ee resolved high-$p_{\mathrm{T}t}$	2.8	$^{+3.9}_{-3.2}$	($^{+3.7}_{-3.1}$	$^{+1.1}_{-0.6}$)
ee merged high-$p_{\mathrm{T}t}$	2.8	$^{+2.2}_{-1.8}$	($^{+2.1}_{-1.8}$	$^{+0.8}_{-0.2}$)
$\mu\mu$ high-$p_{\mathrm{T}t}$	3.7	$^{+2.0}_{-1.7}$	($^{+1.8}_{-1.7}$	$^{+0.8}_{-0.3}$)
ee resolved low-$p_{\mathrm{T}t}$	0.7	±1.3	($^{+1.3}_{-1.2}$	$^{+0.5}_{-0.4}$)
ee merged low-$p_{\mathrm{T}t}$	-0.8	±1.2	(±1.1	$^{+0.3}_{-0.6}$)
$\mu\mu$ low-$p_{\mathrm{T}t}$	1.6	±0.8	($^{+0.8}_{-0.7}$	$^{+0.3}_{-0.2}$)
$H \rightarrow \gamma^*\gamma \rightarrow \ell\ell\gamma$ global fit	1.5	±0.5	(±0.5	$^{+0.2}_{-0.1}$)

Table 4: Systematic uncertainties on the measured signal strength and the measured cross section times branching ratio, in percent. The uncertainties are symmetrized and ordered by impact. The statistical and total uncertainties are shown for comparison.

Source	μ	$\sigma \times \mathcal{B}$
Spurious Signal		6.1
$\mathcal{B}(H \rightarrow \ell\ell\gamma)$	5.8	–
QCD	4.7	1.1
ℓ, γ, jets		4.0
PDF	2.3	0.9
Luminosity		1.7
Pile-up		1.7
Minor prod. modes		0.8
$H \rightarrow \gamma\gamma$ bkg		0.7
Parton Shower		0.3
Total systematic	11	7.9
Statistical		31
Total	33	32